Chen, R., Zhao, T., Wu, W., Wu, F., Li, L., Qian, J., Xu, R., Wu, H., Albishri, H. M., Al-Bogami, A. S., El-Hady, D. A., Lu, J. & Amine, K. (2014). Free-Standing Hierarchically Sandwich-Type Tungsten Disulfide Nanotubes/Graphene Anode for Lithium-Ion Batteries. Nano Letters, 14(10), pp. 5899-5904. doi: 10.1021/nl502848z

Free-standing hierarchically sandwich-type tungsten disulfide nanotubes/graphene anode for lithium-ion batteries

Renjie Chen[a*||], Teng Zhao[a||], Weiping Wu[b], Feng Wu[a*], Li Li[a], Ji Qian[a], Rui Xu[c], Huiming Wu[c], Hassan M. Albishri[d], A. S. Al-Bogami[d], Deia Abd El-Hady[d], Jun Lu[c,*], Khalil Amine[c,d,*].

a Beijing Key Laboratory of Environmental Science and Engineering, School of Chemical Engineering and Environment, Beijing Institute of Technology, Beijing, 100081, China.
B Cambridge Ink Technology Ltd., 91 Devonshire Mews, Devonshire Road, Cambridge, CB1 2BB, United Kingdom
c Chemical Sciences and Engineering Division, Argonne National Laboratory, 9700 South Cass Avenue, Lemont, Illinois 60440, United States
d King Abdulaziz University, Faculty of Science, 80203 Jeddah, Saudi Arabia

ABSTRACT: Transition metal dichalcogenides (TMD), analogue of graphene, could form various dimensionalities. Similar to carbon, one dimensional (1D) nanotube of TMD materials has wide application in hydrogen storage，Li-ion batteries and super-capacitors due to their unique structure and properties. Here we demonstrate the feasibility of tungsten disulfide nanotubes (WS_2-NTs)/graphene (GS) sandwich-type architecture as anode for lithium-ion batteries for the first time. The graphene based hierarchical architecture plays vital roles in achieving fast electron/ion transfer, thus leading to good electrochemical performance. When evaluated as anode, WS_2-NTs /GS hybrid could maintain a capacity of 318.6 mA/g over 500 cycles at a current density of 1A/g. Besides, the hybrid anode does not require any additional polymetric binder, conductive additives or a separate metal current-collector. The relatively high density of this hybrid is beneficial for high capacity per unit volume. Those characteristics make it a potential anode material for light and high performance lithium-ion batteries.

KEYWORDS: Lithium-ion batteries, anode material, graphene, tungsten disulfide nanotube, sandwich-type structure, electro-chemical performance

Rechargeable lithium ion batteries (LIBs) have long been considered as the most effective energy-storage technology and dominated portable electronic market for over two decades.[1, 2] Based on the intercalation mechanism, state-of-the-art Li-ion technology can exhibit a theoretical specific energy of ~400 Wh/kg, such as $LiCoO_2$/graphite system.[3] However, it is urgent to explore new chemistries and materials that can significantly increase the cell energy density, considering the future demand for electronic vehicles and large-scale energy storage plants. [4, 5]

Graphite, a widely used anode material for the current LIBs, has a theoretical capacity of only 372 mAh/g, given a fully intercalated LiC_6 compound, which is one of the limiting factors for achieving high energy density of the cell[6]. In order to overcome such technical bottleneck, considerable effort has been devoted to design and synthesise new anode materials with higher theoretical specific capacity, such as transition metal oxides (SnO_2, Co_3O_4,Fe_3O_4), Sn and Si[7]. However, all these materials suffer from severe volume variation during charge-discharge cycling, which results in serious pulverisation of the electrodes, and thus, rapid capacity degradation. For instance, Si has a high specific capacity of 4200 mAh/g if fully lithiated to $Li_{4.4}Si$, however, it also shows a large volume expansion up to 400%. Such volume expansion causes huge mechanical stress of the electrode, and therefore, severely limits the lifetime of Si anode. Although various strategies have been proposed to enhance the structural stability of Si-based materials, including carbon or polymer coating[8, 9], nano-structuring[10-12] and hierarchical hybridization,[13-15] it is still very challenge to overcome the issue of the inherent volume change of these materials during cycling.

Transition metal dichalcogenides (TMD) MX_2 (M=Mo, Ti, V, and W, X=S or Se)[16, 17] with the similar feature of layered structure as graphite could have great potential for alternative anode materials. In general, MX_2 has strong covalent bonds within layers and weak Van der Waals forces between layers, which provide ideal space for intercalation of lithium ions. For instance, MoS_2 has much larger spacing between neighboring layers (0.615 nm) than that of graphite (0.335 nm) and weak van der Waals forces between the layers, which, in principal, may make the Li^+ diffuse easier. However, certain electrochemical properties of MX_2 can only be achieved in their 1-D or 2-D nanostructured crystals because of the relatively high resistance for Li-ion transport in their bulk form. In addition, the electron conductivity of this type of materials is still too low, which could lead to rapid capacity fading and poor rate performance when using as the anode material in a Li-ion cell. A widely used approach to overcome this problem is to design and optimize nanocomposites for good electrical conductivity, since nanostructured TMD likely allows to increase Li-ion intercalation/de-intercalation due to the high surface area and shorter diffusion path for Li-ion transport.

Among these TMD compound, MoS_2, as the most studied TMD for Li^+ storage today, has received considerable attention as a possible anode candidate for Li-ion cells. For instance, MoS_2-C nanotube[18] and graphene/MoS_2 nano-flake[19] have been reported with significant improvement in cycle life and rate performance by taking advantages of the large electrolyte-electrode interface and reduced ion diffuse pathway. On the other hand, WS_2 with higher intrinsic electrical conductivity than MoS_2[20], which is not studied in detail yet, could be a more suitable candidate as the anode material for Li-ion cells.

Herein, we propose a conceptually new approach to design and fabricate a novel three dimensional WS_2 nanotubes/graphene (WS_2-NTs/GS) hybrid with unique sandwich-type architecture via a simple one-pot hydrothermal reaction. As shown in

Figure 1, WS_2-NTs/GS hybrid was easily prepared by dispersion WS_2-NTs into homogenous graphene oxide (GO) solution and subsequent hydrothermal reaction at controlled PH value for conversion of GO to GS[21]. GS could curl and cross-link to form 3D network during dehydration due to the combination of hydrophobic nature and π-π interactions[22] while WS_2-NT was embedded into the galleries of GS. More importantly, controlling PH of solution by adding appropriate amount of ammonia could further enhance those assemble in a compact manner.[23] The procedure is detailed in the experimental section of the Supporting Information. The unique hybrid could benefit from the synergistic effects of its each component. Specifically, the imbedded WS_2-NTs could effectively prevent GS from complete restacking, thus affording pores and channel for ion diffusion. Meanwhile, the good electrical and mechanical properties of GS could not only enhance the anode conductivity, but also accommodate the volume change of anode during cycling. As a result, WS_2-NTs/GS hybrid exhibited improved cycling stability and rate capability compared with that of WS_2-NTs.

X-ray diffraction (XRD) patterns of WS_2-NTs and WS_2-NTs/GS are shown in Figure 2A. The analysis of WS_2-NTs hybrid spectrum shows highly crystalline hexagonal structure (JCPDS No. 84-1398). For WS_2-NTs/GS hybrid, all the diffraction peaks are consistent with that of WS_2-NTs except for an additional small and broad peak appearing at 2θ of 24~26° (inset). Such peak originates from the (002) plane of GS, indicating a disordered stack of graphene sheet. These results suggest that the attachment of WS_2-NTs on GS does not influence its crystallinity and no new phases are generated.

To further elucidate the effect of the deposition of WS_2-NTs on the microstructure of graphene, Raman spectroscopy was carried out to characterize the carbon lattice in the WS_2-NTs/GS hybrid (Figure 2B). The Raman spectrum of pure graphene (GS) showed a pattern of partially graphitized carbon. The peak at ~1350 cm^{-1} (D band) is assigned to defects and disorder in the graphene layer while peaks at ~1593 cm^{-1} (G band) is related to the coplanar vibration of sp^2-bonded carbon atoms in GS. Interestingly, the intensity of the D band in the WS_2-NTs/GS hybrid is higher than that of the pure GS, indicating a more disordered stack of graphene layer in the hybrid. To some extents, it reveals that the WS_2-NTs were embedded into the interlayer galleries of GS and prevent it from restacking. It should also be noted that the characteristic Raman scattering peaks for WS_2-NTs are mainly observed below 1000 cm^{-1}, which is consistent with the crystalline nature of WS_2-NTs in the hybrid.[24]

To determine the chemical composition of WS_2-NTs/GS hybrid, X-ray photoelectron spectroscopy (XPS) analyses were conducted. According to the broad XPS scan spectrum in the region of 0-1100 eV (Figure 3A), four elements including W, S, C, O are detected and their atomic concentration is 7.55%-W, 13.54%-S, 66.91%-C, 12.00%-O, respectively. The calculated atomic ratio of S to W is ~1.8, closed to the theoretically predicted value for WS_2. The W_{4f} XPS spectra of the hybrid exhibits peaks observed at 33.5 eV and 31.3 eV, corresponding to the $W_{4f5/2}$and $W_{4f7/2}$ characteristic peaks of WS_2-NTs (Figure 3B). As for the peak at 36.9 eV, we assign it to the W-O bond, indicating a low surface oxidation[25]. The presence of WS_2-NTs can be further confirmed by the two distinct S_{2p} peaks at 161.9 eV and 163.2 eV, which correspond to the $S_{2p3/2}$ and $S_{2p1/2}$ components of WS_2-NTs (Figure 3C). Besides, C1s (284.5eV) and O1s (530eV) peaks are mainly attributed to the carbon and oxygen

atom in GS. The deconvolution of the C1s peaks is displayed in Figure 3D. Peaks centred at 286.1, 287.9 eV are attributed to the residual C-O and C=O groups, respectively. Compared with the case of GO[26], the peak intensities of most oxygen containing groups decrease remarkably, indicating the restoration of sp^2 hybridized carbon network. Meanwhile, the O/C ratio was 1:5.6 for the hybrid, which was also consistent with the reduction degree of GO by dehydration mechanism[27]. Accordingly, we can conclude that the hybrid consists of GS and WS_2-NTs, whose content are about 35.4 wt % and 64.6 wt%, respectively.

The morphology and structure of the WS_2-NTs/GS hybrid were characterized by SEM and TEM. The SEM image (Figure 4A) of WS_2-NTs exhibits a uniform one dimensional (1D) structure with diameter of around 60 nm and length of about 5 um. Like carbon nanotubes, such straight structure could easily form bundles, which provide extra lithium intercalation between inter-tubular sites. Figure 4B shows the electron diffraction pattern of two parallel WS_2-NTs. The $\{10\bar{1}0\}$ spots appear to be arranged in a double-hexagonal pattern, corresponding to in plane diffractions in each tube[28]. The HR-TEM image (Figure 4C) of individual WS_2-NTs clearly displays the hollow interior and multi-walls. Compared with straight WS_2-NTs, WS_2-NTs/GS hybrid display a three dimensional (3D) sandwich-like architecture that individual WS_2 nanotubes are homogeneously incorporated into the interlayer galleries of graphene sheets (Figure 4D). From the magnified SEM (inset), we can see that thin graphene could easily wrap around WS_2-NTs due to its flexibility. The microstructure of WS_2-NTs/GS hybrid was further analyzed by HR-TEM (Figure 4D and 4E). It is clear that WS_2-NTs bundles were well dispersed in graphene matrices. According to the cross-sectional images, there are about five layer graphene sheets wrapping around the edges of WS_2-NTs, which have a d-spacing of approximately 0.62 nm twice than that of GS (~0.34 nm). Figure 4G shows the photograph of the black cylinder of the assembled WS_2-NTs/GS hybrid， which can be cut and compressed into circular pellet with a diameter of 11 mm for direct use as anode in standard CR 2025 coin cell.

To investigate the anode performance of the WS_2-NTs/GS hybrid, electrochemical characterization was conducted based on two-electrode coin-type cells (CR 2025) with Li metal as the counter-electrode. Figure 5A shows cyclic voltammograms (CV) of the WS_2-NTs/GS hybrid anode for the initial three cycles between 0.01 and 3.00 V at a scan rate of 0.1 mV/s. In the first cycles, two small cathodic peaks at 1.6 V and 1.5 V are observed, which correspond to the lithium insertion to WS_2 to form Li_xWS_2. The following sharp overlap peak at 0.75 V could be attributed to the subsequent conversion reaction of Li with WS_2 and the formation of a solid electrolyte interlayer (SEI)[29, 30]. The starting cathodic peak at 0.5 V is related to the insertion of Li^+ into graphene, which is also electroactive for lithium storage[31]. During the anodic scan, three oxidation peaks at 1.0, 1.6, 2.2 V are observed, corresponding to the reverse extraction of Li^+ from graphene and Li_xWS_2 host, respectively. From the second cycle onward, the cathodic peak at 0.75 V disappears while the original cathodic peaks at 1.6 V and 1.5 V shift to 2.1 V and 1.8 V, indicating improved reversibility of lithiation and delithiation with cycling. In addition, no obvious changes are observed for the redox peaks, implying that the anode exhibits good electrochemical stability. For comparison, the CV of just WS_2-NTs is shown in Figure S1. It can be seen that the electrochemical behavior of WS_2-NTs is almost the same with that of WS_2-NTs/GS hybrid except the absence of redox

related to the insertion/extraction of Li^+ into/from GS.

Figure 5B shows the galvanostatic charge/discharge profiles of the WS_2-NTs/GS hybrid anode in the 1st, 2nd, 10th and 50th at a current density of 0.1 A/g. The hybrid anode delivers an initial capacity of 996.4 mAh/g and a corresponding charge capacity of 697.7 mAh/g with a first-cycle Coulombic efficiency of ~70.0%. The large discharge capacity is attributed to the formation of SEI layer and the irreversible conversion reaction between Li and WS_2, which are consistent with the above CV analysis. After the initial capacity loss, a high capacity retention upon cycling are observed and the pattern of discharge and charge plateaus remains unchanged. A capacity of 500.2 mAh/g is achieved after 50 cycles. For comparison, pure WS_2-NTs were tested under the same current density as that for the WS_2-NTs/GS hybrid anode (Figure S2). The first discharge and charge capacities for WS_2-NTs anode are 768.5 and 660.8 mAh/g, respectively. And serious capacity decay is observed with cycling, accompanied with the gradual disappearance of discharge plateaus at ~2.0 V. After 50 cycles, the capacity of WS_2-NTs anode dramatically decreases to 202.8 mAh/g.

Figure 5C reveals tenth-cycle discharge capacities of around 692.6, 574.8, 546.2, 393.5 mAh/g at current density of 0.1, 0.2, 0.5, 1.0 A/g, respectively. Besides, the specific capacity of WS_2-NTs/GS hybrid anode could recover to 487.9 mAh/g when the current density is returned to 0.1 A/g. More importantly, the galvanostatic measurements for the WS_2-NTs/GS hybrid anode at increasing rate (inset) show the same pattern of discharge and charge plateaus, indicating good rate performance and rate tolerance. In contrast, pure WS_2-NTs anode exhibits poor capacities and rate capabilities. Even when the current density reduced, the capacity cannot recover its initial level. This difference supports that the 3D hierarchical structure could successfully enhance electronic/ionic transport within the anode, resulting improved electrochemical kinetics, which is further evidenced by the results of EIS (Figure 5D) that the charge-transfer resistance (Rct) values of WS_2-NTs/GS hybrid anode is found to be 37.5 Ω, which is lower than that of WS_2-NTs (52.6 Ω).

Figure 5E compares the long cycle performance of WS_2-NTs and WS_2-NTs/GS hybrid anode at high current density of 1 A/g. In the case of WS_2-NTs/GS hybrid anode, the initial capacity is as high as 886.1 mAh/g and it still maintains a capacity of 318.6 mAh/g after 500 cycles. In contrast, much more capacity decay is observed for WS_2-NTs. The specific capacity dramatically decreases from 695.4 mAh/g to 171.9 mAh/g after 500 cycles. The good cycle performance of WS_2-NTs/GS hybrid anode benefits from the following factors: (1) the incorporation of GS significantly enhances the conductivity of anode; (2) the hybrid 3D architecture consisting of layered WS_2-NTs and GS affords pores and large electrolyte/electrode interface, thus providing channels for Li-ion diffusion and reactive sites for Li-ion intercalation; (3) the flexible GS could effectively accommodate the volume change during cycling.

In summary, we have demonstrated the feasibility of WS_2 nanotube/graphene sandwich-type architecture for good electrochemical performance. To the best of our knowledge, it is the first time for reporting such a conceptual design. Compared with pure WS_2-NTs, the hybrid anode exhibits much improved cycling stability and rate capability without additional polymetric binder, conductive additives or a separate metal current-collector. More importantly, the relatively high density of this hybrid is beneficial for high capacity per unit volume, which offsets its poor operating potential and thus makes it a promising anode material for light and high performance lithium-ion

batteries.

ASSOCIATED CONTENT

Supporting Information

Detail of experimental and additional figures depicting experiment results. This material is available free of charge via the Internet at http://pubs.acs.org.

AUTHOR INFORMATION

Corresponding Author

*E-mail: chenrj@bit.edu.cn, wufeng863@vip.sina.com, junlu@anl.gov and amine@anl.gov

Author Contribution

||R.C. and T.Z. contributed equally to this work.

Notes

The authors declare no competing financial interest.

ACKNOWLEDGMENT

This work was supported by the National Science Foundation of China (NSFC, 21373028), the National 863 Program (2011AA11A256), New Century Educational Talents Plan of Chinese Education Ministry (NCET-12-0050) and Beijing Nova Program (Z121103002512029). This work was also supported by the U.S. Department of Energy under Contract DE-AC0206CH11357 from the Vehicle Technologies Office, Department of Energy, Office of Energy Efficiency and Renewable Energy (EERE) and Division of Materials Science, Basic Energy Sciences, Department of Energy, Office of Science. Argonne National Laboratory, a U.S. Department of Energy Office of Science laboratory, is operated under Contract No. DE-AC02-06CH11357. This project was also funded by the Deanship of Scientific research (DSR), King Abdulaziz University, Jeddah under the HiCi Project(grant No: 11-130-1434HiCi). The authors (HMA, DAE, ASA and KA) thank the DSR for their technical and financial support. The authors also acknowledge the U.S.-China Electric Vehicle and Battery Technology Collaboration between Argonne National Laboratory and Beijing Institute of Technology.

References

1. Armand, M.; Tarascon, J. M. *Nature* **2008**, *451*, 652-657.
2. Scrosati, B.; Garche, J. *J. Power Sources* **2010**, *195*, 2419-2430.
3. Kang, B.; Ceder, G. *Nature* **2009**, *458*, 190-193.
4. Tarascon, J. M.; Armand, M. *Nature* **2001**, *414*, 359-367.
5. Dunn, B.; Kamath, H.; Tarascon, J.-M. *Science* **2011**, *334*, 928-935.

6. Wu, Y. P.; Rahm, E.; Holze, R. *J. Power Sources* **2003**, *114*, 228-236.
7. Tirado, J. L. *Mat. Sci. Eng. R* **2003**, *40*, 103-136.
8. Wang, C.; Wu, H.; Chen, Z.; McDowell, M. T.; Cui, Y.; Bao, Z. *Nat. Chem.* **2013**, *5*, 1042-1048.
9. Chen, Z.; Zhou, M.; Cao, Y.; Ai, X.; Yang, H.; Liu, J. *Adv. Energy Mater.* **2012**, *2*, 95-102.
10. Bruce, P. G.; Scrosati, B.; Tarascon, J.-M. *Angew. Chem. Int. Ed.* **2008**, *47*, 2930-2946.
11. Chan, C. K.; Peng, H.; Liu, G.; McIlwrath, K.; Zhang, X. F.; Huggins, R. A.; Cui, Y. *Nat. Nanotechnol.* **2008**, *3*, 31-35.
12. Arico, A. S.; Bruce, P.; Scrosati, B.; Tarascon, J.-M.; van Schalkwijk, W. *Nat. Mater.* **2005**, *4*, 366-377.
13. Magasinski, A.; Dixon, P.; Hertzberg, B.; Kvit, A.; Ayala, J.; Yushin, G. *Nat. Mater.* **2010**, *9*, 353-358.
14. Zhou, G.; Wang, D.-W.; Li, F.; Zhang, L.; Li, N.; Wu, Z.-S.; Wen, L.; Lu, G. Q.; Cheng, H.-M. *Chem. Mater.* **2010**, *22*, 5306-5313.
15. Wang, H.; Cui, L.-F.; Yang, Y.; Sanchez Casalongue, H.; Robinson, J. T.; Liang, Y.; Cui, Y.; Dai, H. *J. Am. Chem. Soc.* **2010**, *132*, 13978-13980.
16. Ghorbani-Asl, M.; Zibouche, N.; Wahiduzzaman, M.; Oliveira, A. F.; Kuc, A.; Heine, T. *Sci. Rep.* **2013**, *3*, 2961.
17. Zak, A.; Feldman, Y.; Lyakhovitskaya, V.; Leitus, G.; Popovitz-Biro, R.; Wachtel, E.; Cohen, H.; Reich, S.; Tenne, R. *J. Am. Chem. Soc.* **2002**, *124*, 4747-4758.
18. Zhang, C.; Wang, Z.; Guo, Z.; Lou, X. W. *ACS Appl. Mater. Inter.* **2012**, *4*, 3765-3768.
19. Yu, H.; Ma, C.; Ge, B.; Chen, Y.; Xu, Z.; Zhu, C.; Li, C.; Ouyang, Q.; Gao, P.; Li, J.; Sun, C.; Qi, L.; Wang, Y.; Li, F. *Chem.-Eur. J.* **2013**, *19*, 5818-5823.
20. Zhang, C.; Ning, Z.; Liu, Y.; Xu, T.; Guo, Y.; Zak, A.; Zhang, Z.; Wang, S.; Tenne, R.; Chen, Q. *Appl.Phys.Lett.* **2012**, *101*, 113112.
21. Xu, Y.; Sheng, K.; Li, C.; Shi, G. *ACS Nano* **2010**, *4*, 4324-4330.
22. Zhou, G.; Yin, L. C.; Wang, D. W.; Li, L.; Pei, S.; Gentle, I. R.; Li, F.; Cheng, H. M. *ACS Nano* **2013**, *7*, 5367-5375.
23. Bi, H.; Yin, K.; Xie, X.; Zhou, Y.; Wan, N.; Xu, F.; Banhart, F.; Sun, L.; Ruoff, R. S. *Adv. Mater.* **2012**, *24*, 5124-5129.
24. Krause, M.; Virsek, M.; Remškar, M.; Kolitsch, A.; Möller, W. *Phys. Status Solidi B* **2009**, *246*, 2786-2789.
25. Ratha, S.; Rout, C. S. *Acs Applied Materials & Interfaces* **2013**, *5*, 11427-11433.
26. Dreyer, D. R.; Park, S.; Bielawski, C. W.; Ruoff, R. S. *Chem. Soc. Rev.* **2010**, *39*, 228-240.
27. Liao, K. H.; Mittal, A.; Bose, S.; Leighton, C. S.; Mkhoyan, K. A.; Macosko, C. M. *ACS Nano* **2011**, *5*, 1253-1258.
28. Whitby, R. L. D.; Hsu, W. K.; Fearon, P. K.; Billingham, N. C.; Maurin, I.; Kroto, H. W.; Walton, D. R. M.; Boothroyd, C. B.; Firth, S.; Clark, R. J. H.; Collison, D. *Chem. Mater.* **2002**, *14*, 2209-2217.
29. Liu, H.; Su, D.; Wang, G.; Qiao, S. Z. *J. Mater. Chem.* **2012**, *22*, 17437-17440.
30. Wang, S.; Li, G.; Du, G.; Li, L.; Jiang, X.; Feng, C.; Guo, Z.; Kim, S. *Nanoscale Res. Lett.* **2010**, *5*, 1301-1306.
31. Wang, G.; Shen, X.; Yao, J.; Park, J. *Carbon* **2009**, *47*, 2049-2053.

Figure Captions:

Figure 1. Schematic illustration of the fabrication of 3D hierarchically structured WS_2-NT/GS hybrid.

Figure 2. (A) XRD patterns of WS_2-NTs and WS_2-NTs/GS hybrid; (B) Raman spectra of WS_2-NTs/GS hybrid with those of WS_2-NT and GS.

Figure 3. XPS spectra of WS_2-NTs/GS hybrid: (A) broad scan spectrum; (B) W4f; (C) S2p; (D) C1s.

Figure 4. (A) and (D) SEM images of WS_2-NTs and WS_2-NTs/GS hybrid; (B) and (C) HR-TEM images of WS_2-NTs; (E) and (F) HR-TEM images of WS_2-NTs/GS hybrid; (G) photography of WS_2-NTs/GS hybrid and schematic illustration of the fabrication WS_2-NTs/GS anode in standard CR 2025 coin cell.

Figure 5. (A) Cyclic voltammetry of the WS_2-NTs/GS hybrid anode over a voltage range of 0.01−3.00 V at a scanning rate of 0.1 mV/s; (B) Discharge/charge voltage profiles of WS_2-NTs/GS hybrid anode at a current density of 100 mA/g; (C) rate capabilities of WS_2-NTs/GS hybrid and WS_2-NTs anode, inset: discharge/charge voltage profiles of WS_2-NTs/GS hybrid at current density of 0.1, 0.2, 0.5, 1 A/g; (D) Nyquist plots of the WS_2-NTs/GS hybrid and WS_2-NTs anode at open potential before cycling; (E) Cycling stability of WS_2-NTs/GS hybrid and WS_2-NTs anode at 1 A /g for 500 cycles.

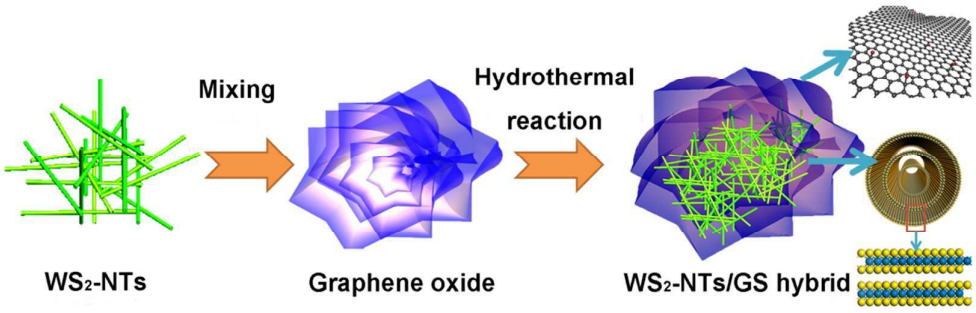

Figure 1. Schematic illustration of the fabrication of 3D hierarchically structured WS_2-NT/GS hybrid.

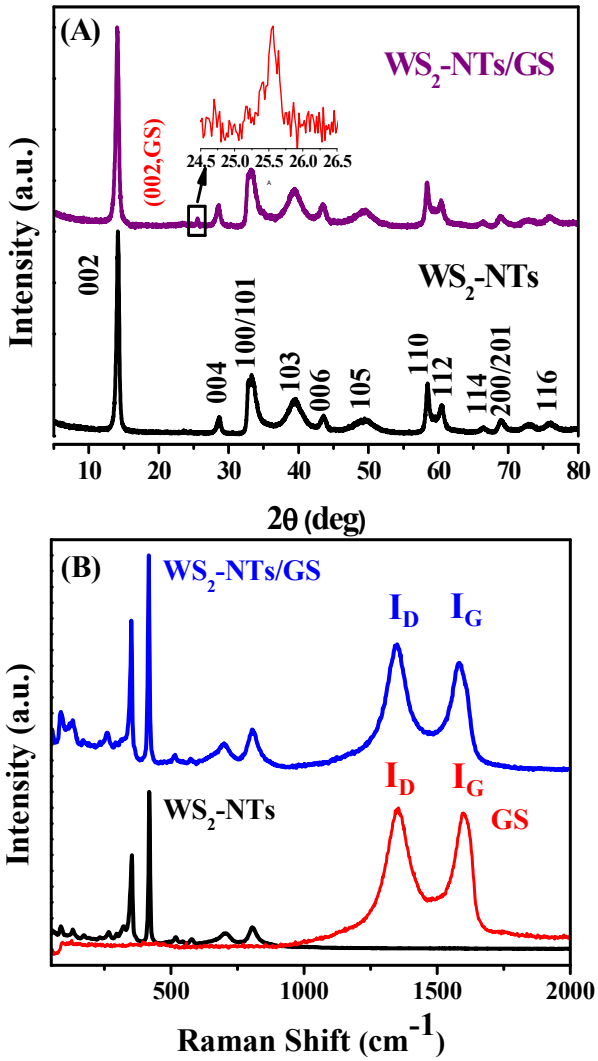

Figure 2. (A) XRD patterns of WS_2-NTs and WS_2-NTs/GS hybrid; (B) Raman spectra of WS_2-NTs/GS hybrid with those of WS_2-NT and GS.

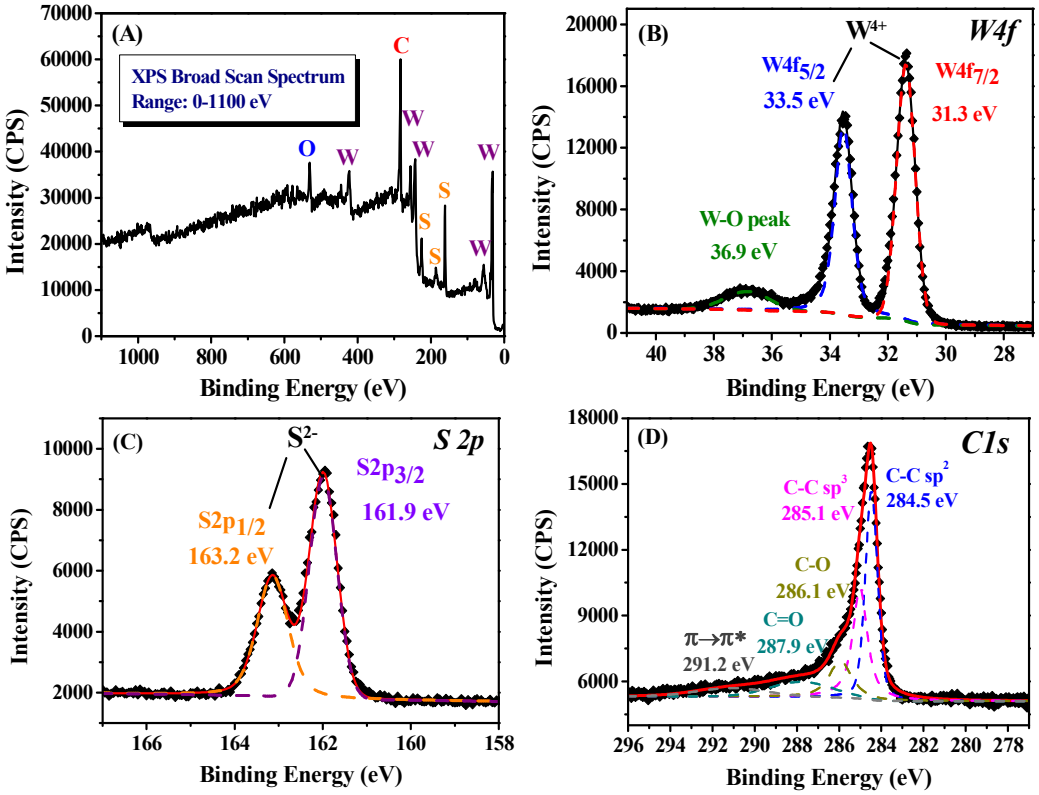

Figure 3. XPS spectra of WS_2-NTs/GS hybrid: (A) broad scan spectrum; (B) W4f; (C) S2p; (D) C1s.

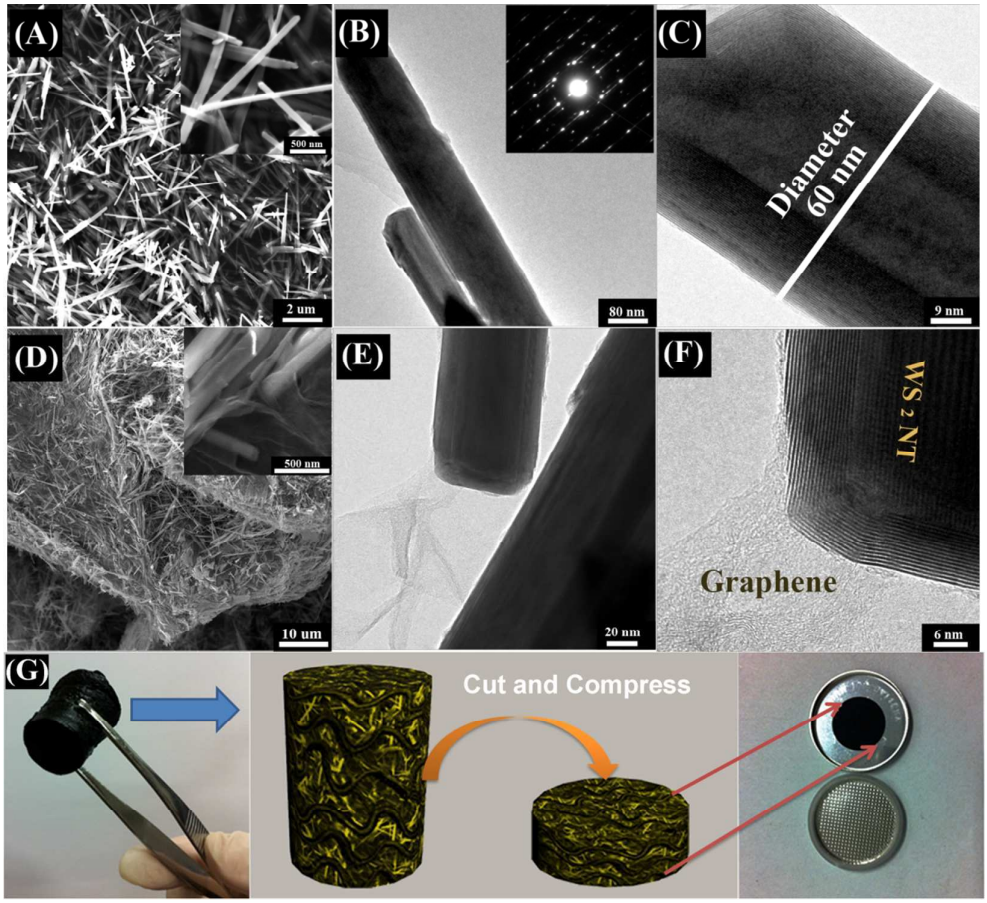

Figure 4. (A) and (D) SEM images of WS_2-NTs and WS_2-NTs/GS hybrid; (B) and (C) HR-TEM images of WS_2-NTs; (E) and (F) HR-TEM images of WS_2-NTs/GS hybrid; (G) photography of WS_2-NTs/GS hybrid and schematic illustration of the fabrication WS_2-NTs/GS anode in standard CR 2025 coin cell.

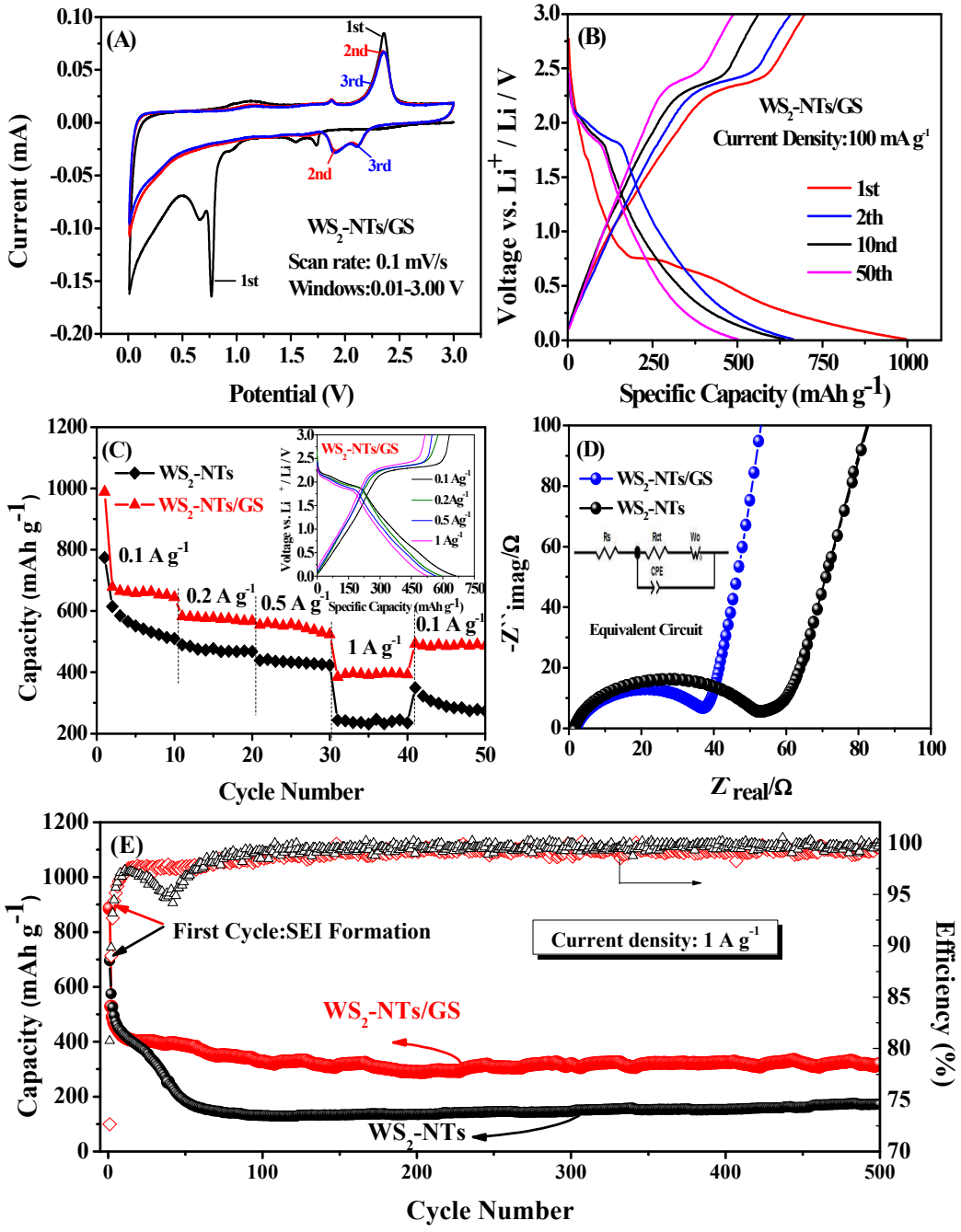

Figure 5 (A) Cyclic voltammetry of the WS_2-NTs/GS hybrid anode over a voltage range of 0.01−3.00 V at a scanning rate of 0.1 mV/s; (B) Discharge/charge voltage profiles of WS_2-NTs/GS hybrid anode at a current density of 100 mA/g; (C) rate capabilities of WS_2-NTs/GS hybrid and WS_2-NTs anode, inset: discharge/charge voltage profiles of WS_2-NTs/GS hybrid at current density of 0.1, 0.2, 0.5, 1 A/g; (D) Nyquist plots of the WS_2-NTs/GS hybrid and WS_2-NTs anode at open potential before cycling; (E) Cycling stability of WS_2-NTs/GS hybrid and WS_2-NTs anode at 1 A /g for 500 cycles.

TOC

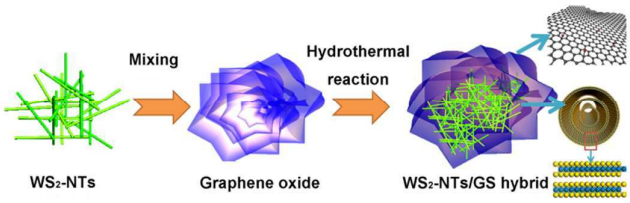
Mixing
Hydrothermal
reaction
WS2-NTs
Graphene oxide
WS2-NTs/GS hybrid